



HAL
open science

Clumped fluoride-hydroxyl defects in forsterite: Implications for the upper-mantle

Céline Crépisson, Marc Blanchard, Hélène Bureau, Chrystèle Sanloup,
Anthony C. Withers, Hicham Khodja, Suzy Surblé, Caroline Raepsaet, Keevin
Béneut, Clémence Leroy, et al.

► **To cite this version:**

Céline Crépisson, Marc Blanchard, Hélène Bureau, Chrystèle Sanloup, Anthony C. Withers, et al..
Clumped fluoride-hydroxyl defects in forsterite: Implications for the upper-mantle. *Earth and Planetary Science Letters*, 2014, 390, pp.287-295. 10.1016/j.epsl.2014.01.020 . hal-00959948

HAL Id: hal-00959948

<https://hal.science/hal-00959948>

Submitted on 17 Mar 2014

HAL is a multi-disciplinary open access archive for the deposit and dissemination of scientific research documents, whether they are published or not. The documents may come from teaching and research institutions in France or abroad, or from public or private research centers.

L'archive ouverte pluridisciplinaire **HAL**, est destinée au dépôt et à la diffusion de documents scientifiques de niveau recherche, publiés ou non, émanant des établissements d'enseignement et de recherche français ou étrangers, des laboratoires publics ou privés.

23 **Abstract**

24 The mechanism and magnitude of fluorine incorporation in H-bearing forsterite were
25 investigated through a combined experimental and theoretical approach. Forsterite samples
26 were synthesized in a piston cylinder press at 2 and 4 GPa, in hydrous conditions, with or
27 without fluorine. High fluorine solubilities of 1715 and 1308 ppm F were measured by
28 particle induced gamma-ray emission (PIGE) in forsterites synthesized at 2 and 4 GPa,
29 respectively. In addition, first-principles calculations based on density functional theory were
30 performed in order to investigate the coupled incorporation mechanisms of fluorine and water
31 in forsterite. Our results demonstrate the close association of fluoride, hydroxyl groups and Si
32 vacancies. Comparison of experimental and theoretical infrared absorption spectra enables
33 assignment of the nine OH stretching bands ($3500\text{-}3700\text{ cm}^{-1}$) observed in F-rich synthetic
34 forsterite to clumped fluoride-hydroxyl defects in the forsterite crystal structure.
35 Noteworthy, similar bands were previously recorded on some natural olivine with
36 $\text{Mg}/(\text{Mg}+\text{Fe})$ molar ratio down to 0.86. Fluorine and water cycles are therefore strongly
37 coupled through the nominally anhydrous minerals and the mantle fluorine budget can be
38 entirely accommodated by these mineral phases.

39

40

41 **1. Introduction**

42 Very little is known about the deep fluorine cycle. The presence of fluorine in volcanic
43 gases and melt inclusions shows that there is a fluorine flux from the depth to the surface
44 (Schilling et al., 1980; Aoki et al., 1981; Symonds et al., 1988; Bureau et al., 1998; Pyle and
45 Mathers, 2009). Fluxes from surface to depth are also expected at subduction zones, where
46 serpentinites are the most likely carrier of halogen elements including fluorine (John et al.,
47 2011 and references therein). Fluorine released from the dehydration of the oceanic crust can
48 be degassed during through arc volcanism or may be recycled back into the mantle with an
49 efficiency of around 95% (Straub and Layne, 2003; John et al., 2011). Significant fluorine
50 enrichments in mantle rocks are suggested by elevated concentrations (0.2 wt%) in some
51 kimberlite samples (Paul et al., 1975) and by the identification of "fluoride melts" in a
52 metasomatized mantle xenolith from New Zealand (Klemme, 2004). Estimates of the fluorine
53 concentration of the primitive Earth mantle based on CI carbonaceous chondrite range from
54 15 ppm to 25 ppm (McDonough and Sun, 1995; Palme and Jones, 2003).

55 Little is also known about fluorine incorporation in the solid Earth. For long it has
56 been proposed that the main fluorine carriers were hydrous and minor accessory minerals
57 such as apatite, micas, amphibole (Smith et al., 1981; Smith, 1981) or clinohumite (Brey et
58 al., 2009). The role of nominally anhydrous and fluorine-free silicates as a deep fluorine
59 reservoir has only recently been proposed (Hervig and Bell, 2005; Bromiley and Kohn, 2007;
60 Beyer et al., 2012; Dalou et al., 2012; Bernini et al., 2013; Mosenfelder and Rossman, 2013a,
61 2013b; Fabbrizio et al., 2013). In particular, fluorine solubility in olivine, the main constituent
62 of the upper mantle, could reach 900 ppm (Fabbrizio et al., 2013), 1900 ppm (Bernini et al.,
63 2013) or even 4500 ppm (Bromiley and Kohn, 2007). The incorporation mechanism of
64 fluorine in these nominally anhydrous and fluorine-free silicates remains speculative. Crystal-

65 chemical considerations based on the similar ionic radius of fluoride (0.130 nm) and hydroxyl
66 ions (0.136 nm) suggest that fluoride incorporation could share some similarities with the
67 incorporation of OH groups in these minerals. As a matter of fact, the fluoride for hydroxyl
68 substitution is commonly observed in hydrous minerals (e.g. amphibole, Robert et al., 1999).
69 The substitution has also been reported in some nominally anhydrous silicates, such as garnet
70 (Visser, 1993) and zircon (Caruba et al., 1985; Balan et al., 2013), and in high pressure
71 hydrous phases, such as superhydrous phase B (Hazen et al., 1997).

72 In the present study, we determine the mechanism and magnitude of fluorine
73 incorporation in H-bearing forsterite (Fo100) by experiment and theory. This work is
74 completed by the further investigation (Particle Induced Gamma-ray Emission measurements
75 PIGE) of the synthetic samples from Withers et al. (2011, 2012), which have a composition
76 similar to mantle olivine (Fo90). The results demonstrate the close association of fluoride,
77 hydroxyl groups and Si vacancies. Implications for fluorine storage in the upper mantle are
78 discussed.

79

80 **2. Materials and Methods**

81 *2.1. Syntheses and preparation*

82 Forsterite samples were synthesized in a piston cylinder press at the University of
83 Edinburgh, CSEC. The starting material was prepared by homogenizing a mixture of high
84 purity (reagent grade) reactants (MgO, SiO₂, Mg(OH)₂, and NaF). The Mg/Si molar ratio of
85 the starting material was 1.75, initial H₂O and F contents were ~5 and ~1.1 wt%, respectively.
86 Experiments were performed at 2 GPa (run #PC36F) and 4 GPa (run #PC38 and #PC38F), at
87 ~ 1250°C, in a 3 cm long cell-assembly composed of a graphite heater surrounded by pyrex
88 and talc sleeves. Two welded 5 mm height and 3 mm outer diameter Au₇₅Pd₂₅ capsules, with
89 and without NaF, were simultaneously inserted in the press on top of each other and separated

90 by an alumina disk. MgO powder dried overnight at 1000C was packed around the Au₇₅Pd₂₅
91 capsules. Experiments were run for 3 days and terminated by turning-off the heater before a
92 slow decompression. Temperature was monitored with a Type C thermocouple (W₇₄Re₂₆-
93 W₉₅Re₅) whose extremity was in contact with the top capsule.

94

95 *2.2. Electron microscopy and microprobe analysis*

96 Forsterite grains were mounted on a metallic disk with carbon tape and coated with a
97 10 nm thick carbon film. The texture of the samples was examined with a Zeiss Ultra 55 field
98 emission scanning electron microscope (SEM) with a working distance of 3±0.2 mm and an
99 acceleration voltage of 15 keV. Major elements were analyzed using a Cameca SX FIVE
100 electron microprobe at CAMPARIS facility (UPMC). Acceleration voltage was set to 15 keV,
101 current to 10 nA and beam was focused to 10 µm diameter at the surface of the sample.
102 Counting times were 10 s both on the sample and the background.

103

104 *2.3. Vibrational spectroscopy*

105 IR measurements were done on a Bruker IFS 66v/S Fourier transform infrared
106 spectrometer working in vacuum and aligned in transmission geometry. The sample was
107 disposed in a homemade sample chamber at the focal point of two cassegrainian reflectors.
108 The analysis area of the sample was selected with slits located between the sample and the
109 detector. Every spectrum was acquired in the frequency region 550-9000 cm⁻¹ with resolution
110 of 4 cm⁻¹ and accumulation of 64 scans using the mid infrared instrumental configuration i.e.
111 Globar, KBr and MCT as respectively source, beam splitter and detector. The background
112 was measured after each sample measurement without changing analysis conditions.
113 Absorbance was obtained after subtraction of the baseline using the OPUS/IR software. Seven
114 to ten grains (50 to 150 µm thick) from each capsule were analyzed. After normalization to

115 thickness and subtraction of epoxy signal and baseline, average unpolarized absorption
116 spectra were calculated and fit using Lorentzian line-shapes (Table 1). In the wavenumber
117 range of interest, the epoxy signal corresponds to a strong band at $\sim 3440\text{ cm}^{-1}$, where there is
118 no olivine OH band, plus a weak and broad band centred at $\sim 3550\text{ cm}^{-1}$. The epoxy correction
119 was made for two of the seven spectra of the PC38 synthesis and three of the ten spectra of
120 the PC36F synthesis.

121 Raman spectroscopic measurements were performed with a Renishaw InVia Raman
122 spectrometer coupled with an optical microscope, using a 514.5 nm laser excitation radiation
123 (1 mW power) and a 1200 mm^{-1} grating. Spectra were acquired from 100 to 2200 cm^{-1} , and
124 averaged from 4 accumulations, each with a counting time of 60 s.

125

126 *2.4. Ion beam analysis*

127 Particle induced gamma ray emission (PIGE), Rutherford backscattering spectrometry
128 (RBS) and Elastic Recoil Detection Analysis (ERDA) were performed at the nuclear
129 microprobe of CEA Saclay SIS2M / LEEL (Khodja et al., 2001). In both cases particle
130 induced X-ray emission (PIXE) and Rutherford Backscattering RBS measurements were
131 simultaneously associated to PIGE and ERDA. PIGE is based on the detection of γ -ray
132 emission during a nuclear reaction triggered by a high-energy proton beam and makes it
133 possible to determine accurately fluorine concentrations. The γ -ray emission at 109.9 keV of
134 the $^{19}\text{F}(p,p'\gamma)$ nuclear reaction induced by a 3 MeV proton beam was detected with an HP-Ge
135 detector (Mosbah et al., 1991). ERDA is based on the detection of protons at a low ‘grazing’
136 angle of 15° from a ^4He incident beam of 3 MeV after they have been ejected from the
137 samples through elastic collisions, this method has been recently used to quantify water in
138 nominally anhydrous minerals; details about the procedure are described in (Raepsaet et al.,
139 2008; Bureau et al., 2009, Withers et al., 2012). PIXE and RBS measurements allow chemical

140 characterization of the sample with respect to major and trace elements. RBS measurements
 141 were performed using an annular detector positioned at 170° with respect to the incident beam
 142 direction, in order to monitor the electrostatic charge delivered to the sample. Further details
 143 can be found in Bureau et al. (2009) and Habrioux et al. (2012). All analyses were performed
 144 by scanning a 4 μm × 4 μm microbeam on 100 μm × 100 μm areas.

145 In PIGE analysis, the fluorine concentration is determined by comparison with a reference
 146 sample using the following relation:

$$147 \quad \frac{[X_{sample}]}{[X_{std}]} = \frac{S_{sample}}{S_{std}} \times \frac{A_{sample}}{A_{std}} \times \frac{N_{\omega_{std}}}{N_{\omega_{sample}}} \quad (1)$$

148 where A is the peak area associated with γ -ray transitions observed for element X , S the
 149 stopping power of the sample and N_{ω} the number of protons by solid angle unit delivered to
 150 the selected area. The reference sample was a pantellerite glass with F content of 4200 ppm
 151 and a similar stopping power to the forsterite samples (KE12; Métrich and Rutherford, 1991).
 152 Calibration was verified on a Macusanite glass with known F content of 1.33 wt% determined
 153 by EMPA (Pichavant et al., 1987). Data were processed with the RISMIN software (Daudin et
 154 al., 2003) following the procedure described in Bureau et al. (2009). Statistical errors are
 155 around 10%. A fit of the RBS spectra with the SIMNRA software (Mayer, 1997), using the
 156 olivine matrix composition, enables determination the N_{ω} parameters.

157

158 *2.5. Theoretical methods*

159 Calculations were performed using the theoretical approach and convergence
 160 parameters described in Balan et al. (2011). Calculations are based on the density functional
 161 theory, with the generalized gradient approximation (GGA) to the exchange-correlation
 162 functional as proposed by Perdew, Burke and Ernzerhof (Perdew et al., 1996) and periodic
 163 boundary conditions. Structure relaxations were done on a 2×1×2 supercell (112 atoms) of

164 forsterite using the PWscf code of the Quantum Espresso package (Giannozzi et al., 2009;
165 <http://www.quantum-espresso.org>). The theoretical relaxed primitive orthorhombic-cell
166 parameters of anhydrous forsterite are $a = 4.78 \text{ \AA}$, $b = 10.28 \text{ \AA}$, and $c = 6.01 \text{ \AA}$ ($Pbnm$ space
167 group). The optimized cell parameters of pure forsterite were kept constant during the
168 relaxation of the F- and OH-bearing supercells. During this step, no symmetry constraint was
169 applied to the atomic positions and the forces on atoms were minimized to less than 10^{-4}
170 Ry/a.u. Following the same procedure as Balan et al. (2011) high-frequency OH stretching
171 modes and corresponding IR absorption spectra were calculated from the dynamical matrix,
172 Born effective charge tensors and dielectric tensor, obtained using the density functional
173 perturbation theory (Baroni et al., 2001) as implemented in the Phonon code of the Quantum
174 Espresso package (Giannozzi et al., 2009; <http://www.quantum-espresso.org>).

175

176 **3. Results**

177 *3.1. Chemical composition and infrared spectra of synthetic forsterite samples*

178 The investigated samples consist of transparent and large ($> 100 \text{ \mu m}$) forsterite
179 crystals with no observed inclusions (Fig. 1). Coexisting enstatite crystals are also identified
180 at the top of the capsule by Raman measurements. Major element analyses indicate that the
181 forsterite grains are close to the stoichiometric composition (Table 1). Beside OH defects, the
182 major measured impurity is fluorine. Concentrations of 1715 ppm F and 1308 ppm F are
183 measured by PIGE at 2 GPa (PC36F) and 4 GPa (PC38F) respectively (Table 1). Minor Na
184 concentrations are also detected by PIGE, i.e. 131 ppm Na and 81 ppm Na at 2 GPa (PC36F)
185 and 4 GPa (PC38F) respectively. These Na concentrations do not exceed the typical range of
186 few hundreds of ppm expected for Na in olivine (e.g. Borisov et al., 2008).

187 The OH-stretching infrared absorption spectrum of the F-free forsterite sample
188 (#PC38, Fig. 2) is similar to that reported in previous studies (Lemaire et al., 2004; Bali et al.,

189 2008; Ingrin et al., 2013). It is dominated by the "hydrogarnet-type" defect $(4H)_{Si}^x$ responsible
190 for a cluster of narrow absorption bands in the $3620\text{-}3550\text{ cm}^{-1}$ region (Balan et al., 2011;
191 Umemoto et al., 2011). Two broader bands observed in the same region have been recently
192 attributed to interstitial OH-groups (Ingrin et al., 2013; Balan et al., 2013). Weak and broad
193 bands ascribed to protonated Mg vacancies (e.g. Balan et al., 2011) are observed at 3160 and
194 3220 cm^{-1} ; whereas weak and narrow bands observed between 3300 and 3400 cm^{-1} could be
195 related to trace amounts of trivalent impurities (Berry et al., 2007).

196 The OH-stretching spectra of F-bearing forsterite samples (#PC36F and #PC38F) are
197 similar to each other. They are also similar to the unpolarized spectrum of a F-rich forsterite
198 (900 ppm F) synthesized at 1200°C and 2 GPa by Fabrizio et al. (2013). Although still
199 dominated by a group of intense bands observed in the $3700\text{-}3500\text{ cm}^{-1}$ region, they differ
200 significantly from that of the F-free sample (#PC38). These bands are not observed in F-free
201 forsterite and are rarely seen in natural samples. The most intense band is located at 3570 cm^{-1}
202 with a shoulder at 3555 cm^{-1} . Seven other intense bands occur at 3674 , 3641 , 3624 , 3597 ,
203 3591 , 3535 and 3514 cm^{-1} (Table 1). The 3612 cm^{-1} band related to $(4H)_{Si}^x$ is still visible but
204 very weak (Fig. 2). Small variations in the relative intensities of the F-related bands in
205 #PC36F and #PC38F cannot be considered as significant owing to the limited number of
206 measurements used to build average IR spectra (Fig. 3). Some bands observed here are close
207 in frequency to OH bands reported previously in natural olivine samples and assigned to
208 hydrous nano-inclusions, such as talc, serpentine or Ti-clinohumite (Beran and Libowitzky,
209 2006). Among the defects related to Ti-clinohumite, Ti planar defects give rise to a band at
210 3410 cm^{-1} and the Ti point defect leads to two bands at 3572 and 3525 cm^{-1} (Berry et al.,
211 2005; Balan et al., 2011). In the present spectra (Fig. 2), no bands are observed at 3525 and
212 3410 cm^{-1} , which would suggest the absence of Ti related defects. Furthermore, no significant
213 presence of Ti has been detected by PIXE during the ERDA analysis of the samples. Talc

214 corresponds to an OH band at 3677 cm^{-1} and bands in the range $3640\text{-}3700\text{ cm}^{-1}$ can be
215 referred to serpentine (Beran and Libowitzky, 2006). The two highest bands, observed here at
216 3674 and 3641 cm^{-1} , could then be assigned to talc or serpentine nano-inclusions that would
217 be nearly homogeneously distributed in all crystals sampled from the two experiments but as
218 it will be shown further by the calculations, intrinsic hydroxylated point defects in the crystal
219 structure of F-bearing forsterite can already explain these bands. The significant modifications
220 observed between the F-free and the F-bearing forsterite samples thus suggest that fluoride
221 ions are associated with these OH-bearing defects.

222 Interestingly, the infrared spectrum of the F-rich synthetic forsterite samples is nearly
223 identical to that of a natural F-rich forsterite sample from Pamir, Tadjikistan (Libowitzky and
224 Beran, 1995), here referred to as the Pamir olivine (Fig. 4a). All the bands observed in the
225 synthetic samples are present in the Pamir sample, except a shoulder at 3555 cm^{-1} and the
226 small band at 3612 cm^{-1} related to $(4\text{H})_{\text{Si}}^{\text{x}}$ defects. Noteworthy, other natural olivine samples
227 described in the literature display absorption bands at wavenumbers close to those reported
228 here for the F-bearing synthetic samples (Sykes et al., 1994; Kishina et al., 2001; Bell et al.,
229 2004, Matsyuk and Langer, 2004; Koch-Müller et al., 2006, Mosenfelder et al., 2011). For
230 these natural samples, Mosenfelder et al. (2011) specifically attributed the three bands above
231 3600 cm^{-1} to coupled substitutions of hydroxyl and fluoride.

232 Water contents are 448 ± 90 ppm H_2O in F-free forsterite; 267 ± 53 ppm H_2O and
233 887 ± 124 ppm H_2O in F-rich forsterite samples synthesized at 4 and 2 GPa, respectively
234 (Table 1). As a comparison, Lemaire et al. (2004) measured water contents ranging from 42 to
235 750 ppm in synthetic forsterite synthesized at 2 GPa and Withers et al. (2012) measured a
236 water content of 462 ppm in olivine ($\text{Mg}\# = 90$) synthesized at 3 GPa.

237 Water and fluorine contents are higher for forsterite synthesized at 2 GPa (#PC36F)
238 than at 4 GPa (#PC38F), however a tendency can hardly be defined with only two pressures

239 investigated. Further experiments are needed to define the effect of pressure on simultaneous
240 water and fluorine incorporation in olivine.

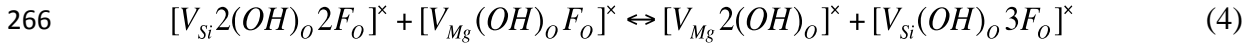
241

242 *3.2. Theoretical results*

243 Infrared spectroscopic measurements suggest that fluoride ions are associated with OH
244 defects in the structure of F-bearing forsterite. Starting from the models of $(4\text{H})_{\text{Si}}^{\times}$ and
245 $(2\text{H})_{\text{Mg}}^{\times}$ defects previously determined by Balan et al. (2011), the structure of fluorinated
246 defects was obtained by substituting fluoride ions for OH groups. The most stable
247 configurations of clumped fluoride and OH defects associated with Si vacancies are displayed
248 in Fig. 4.a. For a single F-for-OH substitution, three configurations of almost equal stability
249 (within $2 \text{ kJ}\cdot\text{mol}^{-1}$) are obtained, denoted as $\text{F}_{(\text{O}1)}$, $\text{F}_{(\text{O}2)}$ and $\text{F}_{(\text{O}3)}$ for F in O1, O2 and O3 site,
250 respectively. Other orientations of OH groups lead to significantly less stable configurations
251 (by $\sim 30 \text{ kJ}\cdot\text{mol}^{-1}$). When two F for OH substitutions are considered, two configurations are
252 found equally stable (within $1.1 \text{ kJ}\cdot\text{mol}^{-1}$): $2\text{F}_{(\text{O}2, \text{O}1)}$ and $2\text{F}_{(\text{O}2, \text{O}3)}$ corresponding respectively
253 to OH/F substitutions in O2 and O1 sites and to OH/F substitutions in O2 and O3 sites. For
254 three F for OH substitutions, the most stable configuration is obtained for F ions located in O2
255 and in the two symmetrical O3 sites ($3\text{F}_{(\text{O}3, \text{O}3, \text{O}2)}$) with the OH group pointing toward the
256 center of the vacancy.

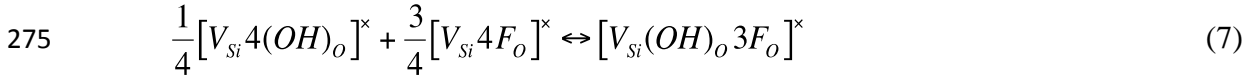
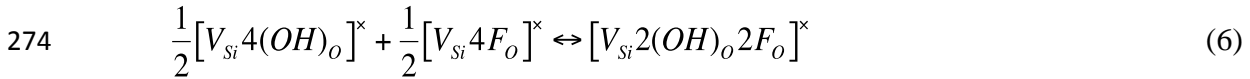
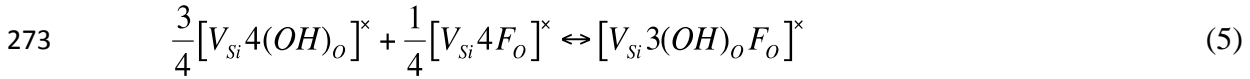
257 For a Mg vacancy, the most stable configuration corresponds to a F substituting for the OH at
258 the O2 site. The position of the remaining OH group in O2 site is almost unchanged. Its OH
259 bond length is slightly shortened (1.000 \AA versus 1.003 \AA in the fully protonated Mg
260 vacancy).

261 Assuming that both Mg and Si vacancies are present in the crystal, the preferential
262 fluorination of Mg or Si vacant sites can be described by three reactions, depending on the
263 number of fluoride ions considered:



267 The total energy difference associated with these three reactions is always significantly
 268 negative (-101 kJ.mol⁻¹, -98 kJ.mol⁻¹ and -81 kJ.mol⁻¹ for reactions 2, 3 and 4, respectively).
 269 This suggests that OH/F substitutions are more likely to occur in Si protonated vacancies than
 270 in Mg protonated vacancies.

271 Similarly, the relative stability of mixed OH/F defects associated to Si vacancies can be
 272 compared to that of equivalent proportions of pure F and OH defects:



276 The total energy difference associated with these reactions is always significantly negative (-
 277 19 kJ.mol⁻¹, -34 kJ.mol⁻¹ and -32 kJ.mol⁻¹ for reactions 5, 6 and 7 respectively). Although the
 278 absolute abundance of mixed OH/F defects also depends on the fluorine activity and H₂O
 279 fugacity, the greater stability of mixed OH/F defects with respect to the defect end-members
 280 is consistent with the weakness of the signal ascribed to fully protonated Si vacancies.

281 The theoretical IR absorption spectrum corresponding to the OH-stretching modes of
 282 the seven most stable geometries of the OH- and F-bearing defects associated with Mg and Si
 283 vacancies have been computed.

284 In the case of an Mg vacancy, one OH/F substitution induces an upshift of the band
 285 from 3222 to 3291 cm⁻¹, compared to the fully protonated Mg vacancy, while the polarization

286 along the z axis remains unchanged (Balan et al., 2011). This frequency shift is directly
287 related to the geometrical changes related to the presence of the fluoride ion.

288 The IR spectra generated for the six most stable configurations of OH/F defects in Si
289 site are displayed in Fig. 4. For one OH/F substitution, each of the three configurations ($F_{(O1)}$,
290 $F_{(O2)}$ and $F_{(O3)}$) lead to three distinct bands (Fig. 4b). The most intense is strongly polarized
291 along x (respectively at 3611, 3583 and 3556 cm^{-1}) whereas the two other bands at lower
292 frequency are polarized along y and z (respectively around 3577, 3534 and 3505 cm^{-1} , with a
293 splitting smaller than 10 cm^{-1}). Most of the bands result from a coupling between 2 or 3 OH-
294 groups of the defects. OH-bands related to two OH/F substitutions fall very close to
295 contributions from the 1 OH/F substitution (Fig. 3c). Configuration $2F_{(O2, O1)}$ leads to one
296 band strongly polarized along x (3581 cm^{-1}) and one band polarized along z (3554 cm^{-1})
297 whereas configuration $2F_{(O2, O3)}$ leads to one band strongly polarized along x (3610 cm^{-1}) and
298 one band polarized equally along x and z (3546 cm^{-1}). All absorption bands arise from
299 coupled vibrational motions of the two OH groups. Finally, $3F_{(O3, O3, O2)}$ is associated with one
300 band at higher frequency (3674 cm^{-1}) strongly polarized along x (Fig. 4d).

301 Lack of polarized measurement prevents a thorough comparison of the theoretical IR
302 spectra with the spectrum of the present synthetic F-rich forsterite. However, the 3700-3500
303 cm^{-1} region of the average IR spectrum of the synthetic samples is very similar to the
304 spectrum of the Pamir olivine (Fig. 5a). We thus consider that the theoretical IR spectra can
305 be compared with the polarized spectrum of the Pamir olivine reported on Fig. 5 (Libowitzky
306 and Beran, 1995). We point out that different polarizations for what seems to be single
307 experimental bands on the Pamir olivine spectrum are often explained by theoretically
308 calculated contributions from different defects.

309 The band at 3674 cm^{-1} (band a, Fig. 5) is well explained by the configuration $3F_{(O3, O3,$
310 $O2)}$ which shows a band strongly polarized along x at the same wavenumber. Although the two

311 theoretical frequencies almost coincide at 3610-3611 cm^{-1} , the bands at 3641 and 3624 cm^{-1}
312 (bands b and b') are best explained by the $2F_{(O_2, O_3)}$ and $F_{(O_1)}$ defects, with the main
313 polarization along x and a much smaller polarization along z. The weakly split bands around
314 3597 and 3591 cm^{-1} (bands c and c') can be attributed to contributions from the configurations
315 $2F_{(O_1, O_2)}$ and $F_{(O_2)}$ for the x component and from configuration $F_{(O_1)}$ for the weaker z and y
316 components. The intense band at 3570 cm^{-1} (band d) is well reproduced by configuration $F_{(O_3)}$
317 giving a band at 3556 cm^{-1} with a polarization along x, whereas the contribution along z could
318 arise from the $2F_{(O_1, O_2)}$ defect. Finally, the band e at 3535 cm^{-1} could be related to the
319 configuration $F_{(O_3)}$. However, the polarization properties, relative intensity and band positions
320 of the experimental band e are not well reproduced and this assignment is still very
321 speculative. Furthermore, there are differences between the spectrum of the synthetic
322 forsterite and that of the Pamir olivine with the presence of a band at 3515 cm^{-1} (Fig. 5): the
323 band e could actually turn into a doublet reproduced by the configuration $F_{(O_3)}$ though
324 polarization remains unexplained.

325

326 *3.3. Integrated molar absorption coefficients of OH defects in forsterite*

327 For each configuration we calculate the integrated molar absorption coefficients for F-
328 and OH-bearing defects. Results are given in Figs. 4b, 4c and 4d for F-bearing Si vacancies
329 and we find a value of 135668 cm^{-2} per mol $\text{H}_2\text{O}/\text{L}$ for an Mg defect with one OH/F
330 substitution. These new data are aligned along a similar trend to OH defects in F-free
331 forsterite (Fig. 6), i.e. on a line rather parallel to the general trend from Balan et al. (2008) but
332 with a downward offset of $\sim 50000 \text{ cm}^{-2}$ per mol $\text{H}_2\text{O}/\text{L}$. This shift is consistent with previous
333 findings on F-free forsterite by Balan et al. (2011). Therefore, the molar absorption coefficient
334 derived from F-free olivine by Withers et al. (2012) can also be applied to F-rich olivine.
335 Noteworthy, the $3F_{(O_3, O_3, O_2)}$ defect is not on the same trend as the other defects. Despite a

336 higher frequency, its molar absorption coefficient is close to values obtained for the other
337 defects. This suggests that all Si defects in forsterite can be approximately treated with a
338 single molar absorption coefficient.

339

340 **4. Discussion**

341 *4.1. Clumped OH/F defects in natural olivine samples*

342 The synthetic forsterite samples display a characteristic IR spectrum in the OH
343 stretching-region that we confidently assign to the presence of clumped fluoride-hydroxyl
344 defects. The reported spectra are similar to those of Fabbrizio et al. (2013) and can be
345 observed also in various natural F-rich olivines from crustal environments (Sykes et al., 1994;
346 Libowitzky and Beran, 1995) and in a kimberlite megacryst from Monastery mine with up to
347 47 ppm F (Bell et al., 2004; Mosenfelder et al., 2011, 2013a) and in some olivines from the
348 Udachnaya kimberlite outcrop (Kishina et al., 2001; Matsyuk and Langer, 2004; Koch-Müller
349 et al., 2006). The latter have not yet been analyzed for fluorine, but the presence of melt
350 inclusions with F-rich phases suggests that some F may have been incorporated in the host
351 olivines (Golovin et al., 2007). This indicates that the results of our experiments as well as
352 those from Fabbrizio et al. (2013) are directly applicable to natural conditions. In particular,
353 the Mg/(Mg+Fe) molar ratio, which varies from 86.00 to 99.65 in the natural samples
354 discussed above (Sykes et al., 1994; Libowitzky and Beran, 1995) does not modify the IR OH
355 stretching bands. This is also true for the kimberlitic olivines investigated by Bell et al. (2004)
356 and Mosenfelder et al. (2011). The positions of their OH stretching bands are similar, within 5
357 cm^{-1} , to those reported in the present study for Fe-free samples. Consequently the
358 incorporation mechanisms and solubility of fluorine are not expected to be significantly
359 changed in presence of iron. The present results also indicate that some OH IR bands
360 observed by Sykes et al. (1994) in a boron and fluorine rich olivine (0.33-0.55 wt% F and

361 0.35-0.40 wt% B) could be explained without having to consider F-B coupled substitutions.
362 Additionally FTIR measurements prove to be useful for the identification of F-rich olivine
363 including Fe-rich olivine. It must be noted however that this IR signature is not observed for
364 synthetic hydrous olivines from Withers et al. (2011) and (2012) that contain up to 47 ppm F,
365 despite not having been intentionally doped with fluorine (Table 1). On the other hand, the
366 natural olivines ROM177 and GRR1012-2 containing 37 and 47 ppm F, respectively
367 (Mosenfelder et al., 2013a), display the IR signature assigned here to clumped fluoride-
368 hydroxyl defects. This apparent discrepancy might be explained by the ratio of the fluorine to
369 water contents. With less than 220 ppm H₂O, the fluorine-related defects are still
370 distinguishable by FTIR measurements, whereas in the synthetic olivines containing more
371 water, the F-free hydroxyl defects are dominant.

372 Similar studies on other NAMs may reveal comparable processes, even though first
373 studies on F-bearing pyroxenes (Mosenfelder and Rossman, 2013a and 2013b) have not
374 revealed so far characteristic IR OH stretching bands that could be linked to incorporation of
375 fluorine.

376

377 *4.2. Cooperative solubility of water and fluorine in olivine*

378 In nominally anhydrous silicates, the hydrolytic weakening mechanism consists in an
379 increase of cationic vacancy concentration in presence of water due to a thermodynamic
380 stabilization of the vacancies by the presence of the charge compensating protons (Brodholt
381 and Refson, 2000). Our experimental and theoretical results indicate that mixed OH/F defects
382 display an even greater stability. Therefore, the presence of fluoride ions should contribute to
383 the hydrolytic weakening mechanism. An important consequence of this cooperative effect is
384 that the dependence of water solubility in forsterite on water fugacity should be modified in
385 presence of fluoride. Indeed, this dependence is a function of the number of OH groups

386 associated with a specific OH defect (Keppler and Bolfan-Casanova, 2006). In high pressure
387 F-free forsterite samples, water incorporation is dominated by $(4\text{H})^x_{\text{Si}}$ defects and to a lesser
388 proportion by interstitial defects (Ingrin et al., 2013). Thus, the replacement of $(4\text{H})^x_{\text{Si}}$ defects
389 by clumped F/OH defects should lead to a decrease in the fugacity exponent between the F-
390 free and F-bearing system.

391

392 *4.3. Geodynamical implications*

393 We show that fluorine solubility can reach more than 1300 ppm in hydrous olivine
394 at pressures and temperatures relevant of the upper-mantle. Such high solubility implies that
395 significant amounts of fluorine can be stored in nominally anhydrous minerals in the upper
396 mantle.

397 Our experiments establish the link between F and OH assimilation in mineral networks. This
398 must be particularly true in subduction settings where water is recycled back to the mantle.
399 Indeed, if F and OH are associated, F could be recycled in the mantle together with water
400 through F incorporation in NAMs in a peridotitic layer at the bottom of the down-going
401 oceanic lithosphere. In that case fluorine could be transferred in deeper regions of subduction
402 zones "en route" to the transition zone and lower mantle during deep hydrous mineral
403 transformations in subducted slabs such as in the phase B (Hazen et al., 1997). Furthermore,
404 recent results have demonstrated the capability of the transition zone to contain fluorine
405 through an experimental study of the solubility of fluorine in ringwoodite and wadsleyite
406 (Roberge et al., 2013).

407 To conclude, water and fluorine geodynamical cycles are likely to be strongly connected in
408 the mantle owing to the existence of clumped defects in nominally anhydrous minerals.

409

410 **Acknowledgements**

411 We are grateful to Olivier Beyssac for access to the Raman spectrometer, to Benoit Baptiste
412 for help in the sample preparation, to the CAMPARIS staff who provided help for microprobe
413 analyses and to Guillaume Morard for his assistance. We thank the very efficient LEEL staff
414 who helped us during PIGE session. The SEM facility of IMPMC is supported by Region Ile
415 de France Grant SESAME 2006 NOI-07-593/R, INSU-CNRS, UPMC and ANR grant ANR-
416 07-BLAN-0124-01. High-pressure experiments were supported by an ERC grant to C.S. (FP7
417 grant agreement no. 259649). The theoretical work was performed using HPC resources from
418 GENCI-IDRIS (Grant 2013-i2013041519) and using the IBM iDataPlex cluster of the UPMC.
419 We also thank J. Mosenfelder and an anonymous reviewer who helped us improving the
420 manuscript.

421

422 **References**

- 423 Aoki, K., Ishiwaka, K., Kanisawa, S., 1981. Fluorine Geochemistry of Basaltic Rocks from
424 Continental and Oceanic Regions and Petrogenetic Application. *Contrib. Mineral.*
425 *Petrol.* 76, 53-59.
- 426 Balan, E., Refson, K., Blanchard, M., Delattre, S., Lazzeri, M., Ingrin, J., Mauri, F., Wright,
427 K., Winkler, B., 2008. Theoretical infrared absorption coefficient of OH groups in
428 minerals. *Am. Mineral.* 93, 950–953.
- 429 Balan, E., Ingrin, J., Delattre, S., Kovacs, I., Blanchard, M., 2011. Theoretical infrared
430 spectrum of OH-defects in forsterite. *Eur. J. Mineral.* 23, 285–292.
- 431 Balan, E., Yi, H., Blanchard, M., 2013. First-principles study of OH defects in zircon. *Phys.*
432 *Chem. Minerals* 40, 547–554.
- 433 Balan, E., Blanchard, M., Lazzeri M., Ingrin, J., 2013. Contribution of interstitial OH groups
434 to the incorporation of water in forsterite. *Phys. Chem. Minerals* DOI 10.1007/s00269-
435 013-0628-y.
- 436 Bali, E., Bolfan-Casanova, N., Koga K.T., 2008. Pressure and temperature dependence of H
437 solubility in forsterite: An implication to water activity in the Earth interior. *Earth*
438 *Planet. Sci. Lett.* 268, 354-363.
- 439 Baroni, S., Giannozzi. P., 2001. Phonons and related properties of extended systems from
440 Density-functionnal perturbation theory. *Rev. Mod. Phys.* 73, 515–562.
- 441 Bell, D.R., Rossman, G.R., 1992. Water in Earth's Mantle: the role of Nominally Anhydrous
442 Minerals. *Science* 255, 1391-1397.

- 443 Bell, D.R., Rossman, G.R., Moore, R.O., 2004. Abundance and Partitioning of OH in a High-
444 pressure Magmatic System: Megacrysts from the Monastery Kimberlite, South Africa.
445 *J. Pet.* 45, 1539-1564.
- 446 Beran, A., Libowitzky, E., 2006. Water in natural mantle minerals. II. Olivine, garnet and
447 accessory minerals. *Rev. Mineral. Geochem.* 62, 169-191.
- 448 Bernini, D., Wiedenbeck, M., Dolejs, D., Keppler, H., 2013. Partitioning of halogens between
449 mantle minerals and aqueous fluids: implications for the fluid flow regime in
450 subduction zones. *Contrib. Mineral. Petrol.* 165, 117–128.
- 451 Berry, A.J., Hermann, J., O'Neill, H.S.C., Foran, G.J., 2005. Fingerprinting the water site in
452 mantle olivine. *Geology* 33, 869-872.
- 453 Berry, A.J., O'Neill, H.St.C., Hermann, J., Scott, D.R., 2007. The infrared signature of water
454 associated with trivalent cations in olivine. *Earth Planet. Sci. Lett.* 261, 134–142.
- 455 Beyer, C., Klemme S., Wiedenbeck, M., Stracke, A., Vollmer, C., 2012. Fluorine in
456 nominally fluorine-free mantle minerals: Experimental partitioning of F between
457 olivine, orthopyroxene and silicate melts with implications for magmatic processes.
458 *Earth Planet. Sci. Lett.* 337-338, 1-9.
- 459 Borisov, A., Pack, A., Kropf, A., Palme, H., 2008. Partitioning of Na between olivine and
460 melt: An experimental study with application to the formation of meteoritic Na₂O-rich
461 chondrule glass and refractory forsterite grains. *Geochim. Cosmochim. Acta* 72,
462 5558–5573.
- 463 Brey, G.P., Bulatov, V.K., Girnis, A.V., 2009. Influence of water and fluorine on melting of
464 carbonated peridotite at 6 and 10 GPa. *Lithos* 112, 249–259.

465 Brodholt, J.P., Refson, K., 2000. An ab initio study of hydrogen in forsterite and a possible
466 mechanism for hydrolytic weakening. *Journal of geophysical research* 105 B8, 18977-
467 18982 .

468 Bromiley, D.W., Kohn, S.C., 2007. Comparisons between fluoride and hydroxide
469 incorporation in nominally anhydrous and fluorine-free mantle minerals. *Goldschmidt*
470 *Conference Abstracts* A124.

471 Bureau, H., Métrich, N., Pineau, F., Semet, P., 1998. Magma–conduit interaction at Piton de
472 la Fournaise volcano (Réunion Island): a melt and fluid inclusion study. *J. Volcanol.*
473 *Geotherm. Res.* 84, 39-60.

474 Bureau, H., Raepsaet, C., Khodja, H., Carraro, A.C., Aubaud, C., 2009. Determination of
475 hydrogen content in geological samples using elastic recoil detection analysis
476 (ERDA). *Geochim. Cosmochim. Acta* 73, 3311–3322.

477 Caruba, R., Baumer, A., Ganteaume, M., Iacconi, P., 1985. An experimental study of
478 hydroxyl groups and water in synthetic and natural zircons: a model of the metamict
479 state. *Am. Miner.* 70, 1224-1231.

480 Dalou, C., Koga, K.T., Shimizu, N., Boulon, J., Devidal, J.L., 2012. Experimental
481 determination of F and Cl partitioning between lherzolite and basaltic melt. *Contrib.*
482 *Mineral. Petrol.* 163, 591-609.

483 Daudin, L., Khodja, H., Gallien, J.P., 2003. Development of “position–charge–time” tagged
484 spectrometry for ion beam microanalysis. *Nuclear Instruments and Methods in Physics*
485 *Research B* 10, 153-158.

486 Fabrizio, A., Stalder, R., Hametner, K., Günther, N., Marquardt, K., 2013. Experimental
487 partitioning of halogens and other trace elements between olivine, pyroxenes,

488 amphibole and aqueous fluid at 2 GPa and 900–1,300 °C. *Contrib. Mineral. Petrol.*
489 DOI 10.1007/s00410-013-0902-5.

490 Frost, D., 2008. The upper mantle and Transition zone. *Elements* 4, 171- 176.

491 Giannozzi, P., Baroni, S., Bonini, N., Calandra, M., Car, R., Cavazzoni, C., Ceresoli, D.,
492 Chiarotti, G. L., Cococcioni, M., Dabo, I., Dal Corso, A., de Gironcoli, S., Fabris, S.,
493 Fratesi, G., Gebauer, R., Gerstmann, U., Gougoussis, C., Kokalj, A., Lazzeri, M.,
494 Martin-Samos, L., 2009. QUANTUM ESPRESSO: a modular and open-source
495 software project for quantum simulations of materials. *J. Phys. Condens. Matter* 21,
496 395502.

497 Golovin, A.V., Sharygin, V.V., and Pokhilenko, N.P., 2007. Melt Inclusions in Olivine
498 Phenocrysts in Unaltered Kimberlites from the Udachnaya-East Pipe, Yakutia: Some
499 Aspects of Kimberlite Magma Evolution during Late Crystallization Stages.
500 *Petrologiya* 15, 178–195.

501 Habrioux, A., Surblé, S., Berger, P., Khodja, H., D’Affroux, A., Mailley, S., Gutel, T.,
502 Patoux, S., 2012. Nuclear microanalysis of lithium dispersion in LiFePO₄ based
503 cathode materials for Li-ion batteries. *Nuclear Instruments and Methods in Physics*
504 *Research B* 290, 13-18.

505 Hazen, M., Yang, H., Prewitt, C.T., Gasparik, T., 1997. Crystal chemistry of superfluorous
506 phase B (Mg₁₀Si₃O₁₄F₄): Implications for the role of fluorine in the mantle. *Am.*
507 *Mineral.* 82, 647-650.

508 Hervig, R. L., Bell, D. R., 2005. Fluorine and Hydrogen in Mantle Megacrysts. *AGU Fall*
509 *Meeting* pp. V41A-1426.

510 Ingrin, J., Liu, J., Depecker, C., Kohn, S.C., Balan, E., Grant, K.J., 2013. Low-temperature
511 evolution of OH bands in synthetic forsterite, implication for the nature of H defects at
512 high pressure. *Phys. Chem. Minerals* 40, 499-510.

513 John, T., Scambelluri, M., Frische, M., Barnes, J.D., Bach, W., 2011. Dehydration of
514 subducting serpentinite: Implications for halogen mobility in subduction zones and the
515 deep halogen cycle. *Earth Planet. Sci. Lett.* 308, 65-76.

516 Kawamoto, T., 2006. Hydrous phases and water transport in the subducting slab. *Reviews in*
517 *Mineralogy and Geochemistry* 62, 273-289.

518 Keppler, H., Bolfan-Casanova, N., 2006. Thermodynamics of water solubility and
519 partitioning. *Reviews in Mineralogy and Geochemistry* 62, 193-230.

520 Khodja, H., Berthoumieux, E., Daudin, L., Gallien, J-P., 2001. The Pierre Süe Laboratory
521 nuclear microprobe as a multi-disciplinary analysis tool. *Nuclear Instruments and*
522 *Methods in Physics Research B* 181, 83-86.

523 Kishina, N.P., Wirth, R., Andrut, M., Ukanov, A.V., 2001. Extrinsic and intrinsic mode of
524 oxygen occurrence in natural olivines : a FTIR and TEM investigation. *Phys. Chem.*
525 *Minerals* 28, 291-301.

526 Klemme, S., 2004. Evidence for fluoride melts in Earth's mantle formed by liquid
527 immiscibility. *Geology* 32, 441-444.

528 Koch-Müller, M., Matsyuk, S.S., Rhede, D., Wirth, R., Kishina, N., 2006. Hydroxyl in mantle
529 olivine xenocrysts from the Udachnaya kimberlite pipe. *Phys. Chem. Minerals* 33,
530 276-287.

- 531 Lemaire, C., Kohn S.C., Brooker, R.A., 2004. The effect of silica activity on the incorporation
532 mechanisms of water in synthetic forsterite: a polarised infrared spectroscopic study.
533 *Contrib. Mineral. Petrol.* 147, 48-57.
- 534 Libowitzky, E., Beran, A., 1995. OH Defects in Forsterite. *Phys. Chem. Minerals* 22, 387-
535 392.
- 536 Matsyuk, S.S., Langer, K., 2004. Hydroxyl in olivines from mantle xenoliths in kimberlites of
537 the Siberian platform. *Contrib. Mineral. Petrol.* 147, 413-437.
- 538 Mayer, M., 1997. SIMNRA User's Guide. Report IPP 9/113, Max-Planck-Institut für
539 Plasmaphysik, Garching, Germany.
- 540 McDonough, W.F., Sun, S.S., 1995. The composition of the Earth. *Chem. geol.* 120,223-253.
- 541 Métrich, M., Rutherford, M.J., 1991. Experimental study of chlorine behavior in hydrous
542 silicic melts. *Geochim. Cosmochim. Acta* 56, 607-616.
- 543 Mosbah, M., Métrich, N., Massiot, P., 1991. PIGME fluorine determination using a nuclear
544 microprobe with application to glass inclusions. *Nuclear Instruments and Methods in*
545 *Physics Research B*58, 227-231.
- 546 Mosenfelder, J.L., Le Voyer, M., Rossman, G.R., Guan, Y., Bell, D.R., Asimow, P., Eiler, J.,
547 2011. Analysis of hydrogen in olivine by SIMS: Evaluation of standards and protocol.
548 *Am. Mineral.* 96, 1725–1741.
- 549 Mosenfelder, J.L., Rossman G.R., 2013a. Analysis of hydrogen and fluorine in pyroxenes: I
550 Orthopyroxene. *Am. Mineral.* 98, 1026–1041.
- 551 Mosenfelder, J.L., Rossman, G.R., 2013b. Analysis of hydrogen and fluorine in pyroxenes: II
552 Clinopyroxene. *Am. Mineral.* 98, 1042–1054.

553 Palme, H., Jones, A., 2003. Solar system abundances of the elements. Treatise on
554 geochemistry 1, 41-61.

555 Paul, D.K., Buckley, F., Nixon, P.H., 1976. Fluorine and Geochemistry of Kimberlites. Chem.
556 Geol. 17, 125-133.

557 Perdew, J.P., Burke, K., Ernzerhof, M., 1996. Generalized Gradient Approximation Made
558 Simple. Phys. Rev. Lett. 77, 3865-3868.

559 Pyle, D.M., Mather, T.A., 2009. Halogens in igneous processes and their fluxes to the
560 atmosphere and oceans from volcanic activity: A review. Chemical Geology 263, 110-
561 121.

562 Raepsaet, C., Bureau, H., Khodja, H., Aubaud, C., Carraro, A., 2008. μ -ERDA developments
563 in order to improve the water content determination in hydrous and nominally anhydrous
564 mantle phases. Nuclear Instruments & Methods in Physics Research Section B-Beam
565 Interactions with Materials and Atoms, 266: 1333-1337.

566 Roberge, M., Bureau H., Bolfan-Casanova, N., Frost, D.J., Raepsaet, C., Surblé, S., Khodja,
567 H., Fiquet, G., 2013. F and Cl solubilities in wadsleyite and ringwoodite. Goldschmidt
568 Conference, Florence, August 26-31, Italy.

569 Robert, J.L., Della Ventura, G., Hawthorne, H.C., 1999. Near-infrared study of short-range
570 disorder of OH and F in monoclinic amphiboles. Am. Mineral. 84, 86-91.

571 Schilling, J.G., Bergeron, M.B., Evans, R., 1980. Halogens in the mantle beneath the North
572 Atlantic. Phil. Trans. R. Soc. Lond. A 29, 147-178.

573 Smith, J.V., Delaney, J.S., Hervig, R.L., Dawson, J.B., 1981. Storage of F and Cl in the upper
574 mantle: geochemical implications. Lithos 14, 133-147.

575 Smith, J.V., 1981. Halogen and Phosphorous storage in the Earth. *Nature* 289, 762-765.

576 Straub, S.M., Layn, G.D., 2003. The systematics of chlorine, fluorine, and water in Izu arc
577 front volcanic rocks: Implications for volatile recycling in subduction zones. *Geochim.*
578 *Cosmochim. Acta* 67, 4179–4203.

579 Sykes, D., Rossman, G., Veblen, D., Grew, E., 1994. Enhanced H and F incorporation in
580 borian olivine. *Am. Mineral.* 79, 904-908.

581 Symonds, R.B., Rose, W.I., Reed, M.H., 1988. Contribution of Cl and F bearing gases to the
582 atmosphere by volcanoes. *Letters to Nature* 334, 415-418.

583 Umemoto, K., Wentzovitsh, R.M., Hirschmann, M.M., Kholstedt, D., Withers, A., 2011. A
584 first-principles investigation of hydrous defects and IR frequencies in forsterite: The case
585 for Si vacancies. *Am. Mineral.* 96, 1475-1479.

586 Visser, D., 1993. Fluorine-bearing Hydrogarnets from Blengsvatn, Bamble Sector, South
587 Norway. *Mineralogy and Petrology* 47, 209-218.

588 Withers, A.C., Hirschmann, M.M., Tenner, T.J., 2011. The effect of Fe on olivine H₂O
589 storage capacity: Consequences for H₂O in the martian mantle. *Am. Mineral.* 96,
590 1039-1053

591 Withers, A.C., Bureau H., Raepsaet, C., Hirschmann, M.M., 2012. Calibration of infrared
592 spectroscopy by elastic recoil detection analysis of H in synthetic olivine. *Chem. Geol.*
593 334, 92-98.

594 Withers, A.C, 2013. On the use of unpolarized infrared spectroscopy for quantitative analysis
595 of absorbing species in birefringent crystals. *Am. Mineral.* 98, 689-697.

596

Table 1

Synthesis conditions, chemical compositions of forsterite samples and positions of the observed absorption bands with their corresponding area and width. Infrared band position, area and full width at half height (FWHH) from fit of the spectra by Lorentzian functions (see text). Detailed polarized IR measurements of samples A710 and M475 are to be found in Withers et al. (2011).

NAME	Mg # ¹	P-T	F (ppm) ²	H ₂ O (ppm) ³	Na (ppm) ²	Band position (cm ⁻¹)	Area (cm ⁻²)	FWHH (cm ⁻¹)
PC36F	100 Mg _{2.02} Si _{10.99} O ₄	2 GPa 1230- 1260°C	1715 (±172) det. lim. = 12	887 (±124)	131(±13) det. lim. = 28	3674.3*	180.78	5.43
						3641.0*	407.08	8.12
						3624.3*	47.27	3.88
						3612.0	10.00	5.00
						3597.1	160.32	7.42
						3591.5	175.51	6.23
						3569.9*	848.61	10.75
						3555.1	27.08	4.08
						3535.1*	277.22	5.62
						3514.7*	47.16	3.76
	3480.7, 3218.2, 3040.0	13.64, 21.5, 27.88	34.50, 36.50, 30.00					
PC38F	100 Mg _{1.99} Si _{11.01} O ₄	4 GPa 1240- 1255°C	1308 (±131) det. lim. = 10	267 (±53)	81(±8) det. lim. = 6	3674.4*	38.92	4.57
						3640.8*	200.30	7.68
						3624.2*	45.74	4.74
						3613.1	10.00	5.00
						3597.9	50.79	5.46
						3591.5	158.15	7.73
						3569.9*	516.02	10.36
						3555.0	53.18	6.14
						3536.2*	117.02	6.71
						3514.0*	10.00	5.00
	3480.2, 3347.8, 3322.1, 3212, 3161.0	4.73, 4.89, 1.16, 15, 105	9.76, 9.35, 5.25, 40, 43.78					

NAME	Mg # ¹	P - T	F (ppm) ²	H ₂ O (ppm) ³	Na (ppm) ²	Band position (cm ⁻¹)	Area (cm ⁻²)	FWHH (cm ⁻¹)
PC38	100 Mg _{1.97} Si _{1.01} O ₄	4 GPa	< 13	448 (±90)	< 14	3612.5	58.09	6.58
						3598.8 [†]	50.10	17.15
		1240- 1255°C	det. lim. = 13	det. lim. = 14	3591.0	18.00	9.02	
					3579.1	38.20	9.23	
					3566.8	28.27	9.42	
					3550.6 [†]	12.56	18.35	
					3528.4	42.32	32.31	
					3480.7, 3446.7, 3418.0,	20.1, 10.73, 0.19,	17.29, 13.43, 3.74,	
					3404.0 3388.0, 3347.0,	5.69, 1.22, 10.73,	7.93, 8.45, 13.43,	
					3321.5, 3303.0 3279.0,	6.70, 0.50, 0.10,	11.49, 10.00, 3.00,	
3217.0, 3157.6, 3038.0	17.34, 39.25, 8.28	3.01, 47.24, 31.00						
A710	90.2	3 GPa	46 (±5)	468 (±81)	< 15	3613		
						3597 [†]		
		1250°C	det. lim. = 5	det. lim. = 15	3577			
					3567			
					3538			
					3500, 3477, 3450,			
					3302			
M475	90.3	10 GPa	47 (±5)	2019 (±332)	< 25	3611		
						3597 [†]		
		1250°C	det. lim. = 12	det. lim. = 25	3580			
					3567			
					3550 [†]			
					3475, 3447			

2 ¹ determined by EPMA, ² by PIGE and ³ by ERDA. For IR absorption bands, *indicates F-related bands and [†] possible bands related to OH-
3 interstitials.

4 **Figure 1:**

5 Secondary electron image of forsterite grains (synthesis #PC36F)

6

7 **Figure 2:**

8 Unpolarized average infrared spectra of synthetic forsterite (black dots) and fit of spectra by a
9 sum of Lorentzian functions in grey line (see parameters of the Lorentzian functions in Table
10 1). Lowermost spectrum absorbance is multiplied by a factor of 4 and spectra are offset
11 vertically for clarity.

12

13 **Figure 3:**

14 Unpolarized infrared spectra of forsterite grains derived from the synthesis #PC38F.

15

16 **Figure 4:**

17 a) Structural models of the most stable configurations for OH/F substitutions in Si vacancy
18 investigated by first-principles calculations. In $3F_{(O3, O3, O2)}$, the OH group points toward the
19 center of the vacancy. In $2F_{(O2, O1)}$ the two OH groups point toward the F in O1 site. In $2F_{(O2,$
20 $O3)}$ the OH in O1 site points toward the F in O3 site while the OH in O3 site points toward O
21 in O1 site. In $F_{(O1)}$ all OH groups are pointing toward the F atom. In $F_{(O2)}$ the OH in O1 site
22 points toward the F while the two OH in O3 sites point toward the O1 atom. In $F_{(O3)}$ the OH in
23 O1 site points toward the F while the other two OH point toward O in O1 site. Theoretical
24 polarized IR spectra for one (b), two (c) and three (d) OH/F substitutions. Red vertical lines
25 correspond to the position of the OH bands in the fully protonated Si vacancy (Balan et al.,
26 2011). The integrated molar absorption coefficient of the corresponding OH defects is
27 indicated in the figure's legend (in cm^{-2} per mol $\text{H}_2\text{O/L}$).

28

29 **Figure 5:**

30 a) Polarized IR spectra of Pamir olivine from Libowitzky and Beran (1995) compared to the
31 unpolarized average IR spectrum of run #PC38F. a.b. indicates the absence of the broad
32 shoulder observed in F-rich forsterite samples at $\sim 3555\text{ cm}^{-1}$.

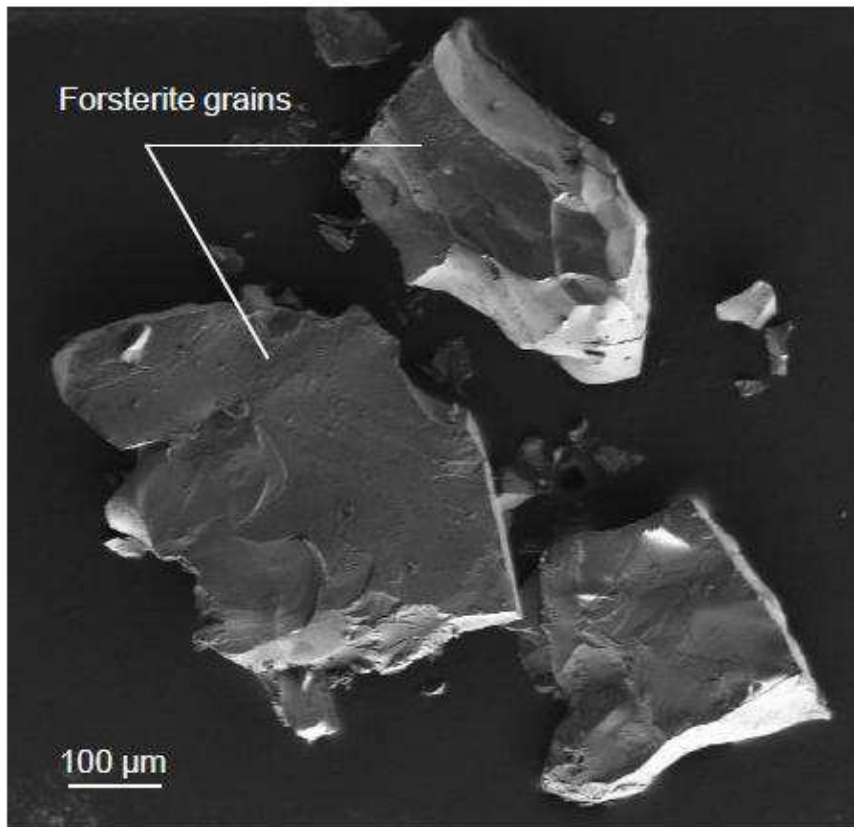
33 b) Calculated polarized spectra considering one, two and three OH/F substitutions in the Si
34 vacancy. Proportions of the various configurations were taken into account following
35 Umemoto et al. (2011) though variation in energy is too weak to induce major changes of
36 relative intensities.

37

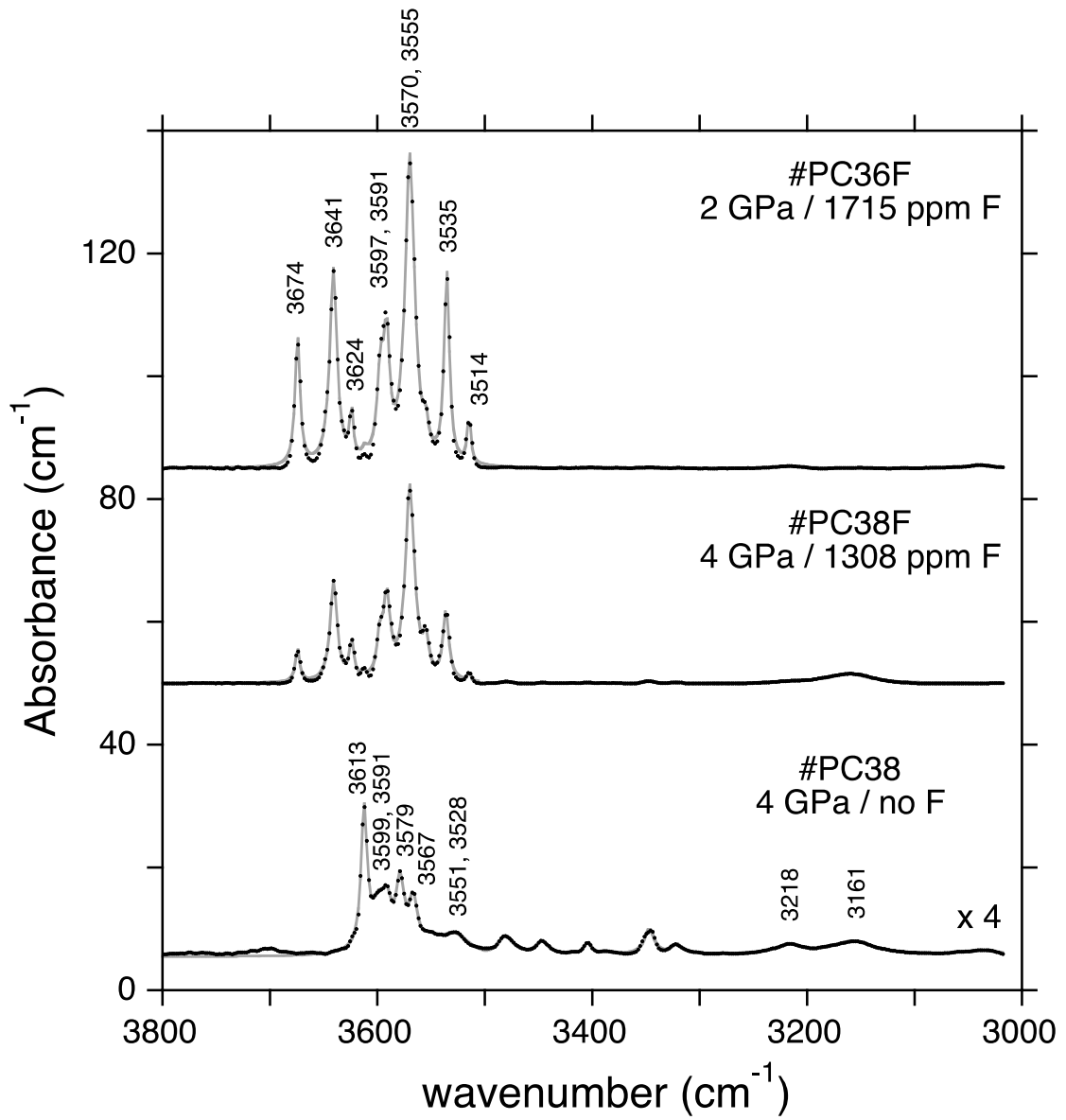
38 **Figure 6:**

39 Theoretical integrated molar absorption coefficients for the different F- and OH-bearing
40 defects. The solid line corresponds to the theoretical correlation obtained by Balan et al.
41 (2010), dashed line is a guide for the eyes.

42

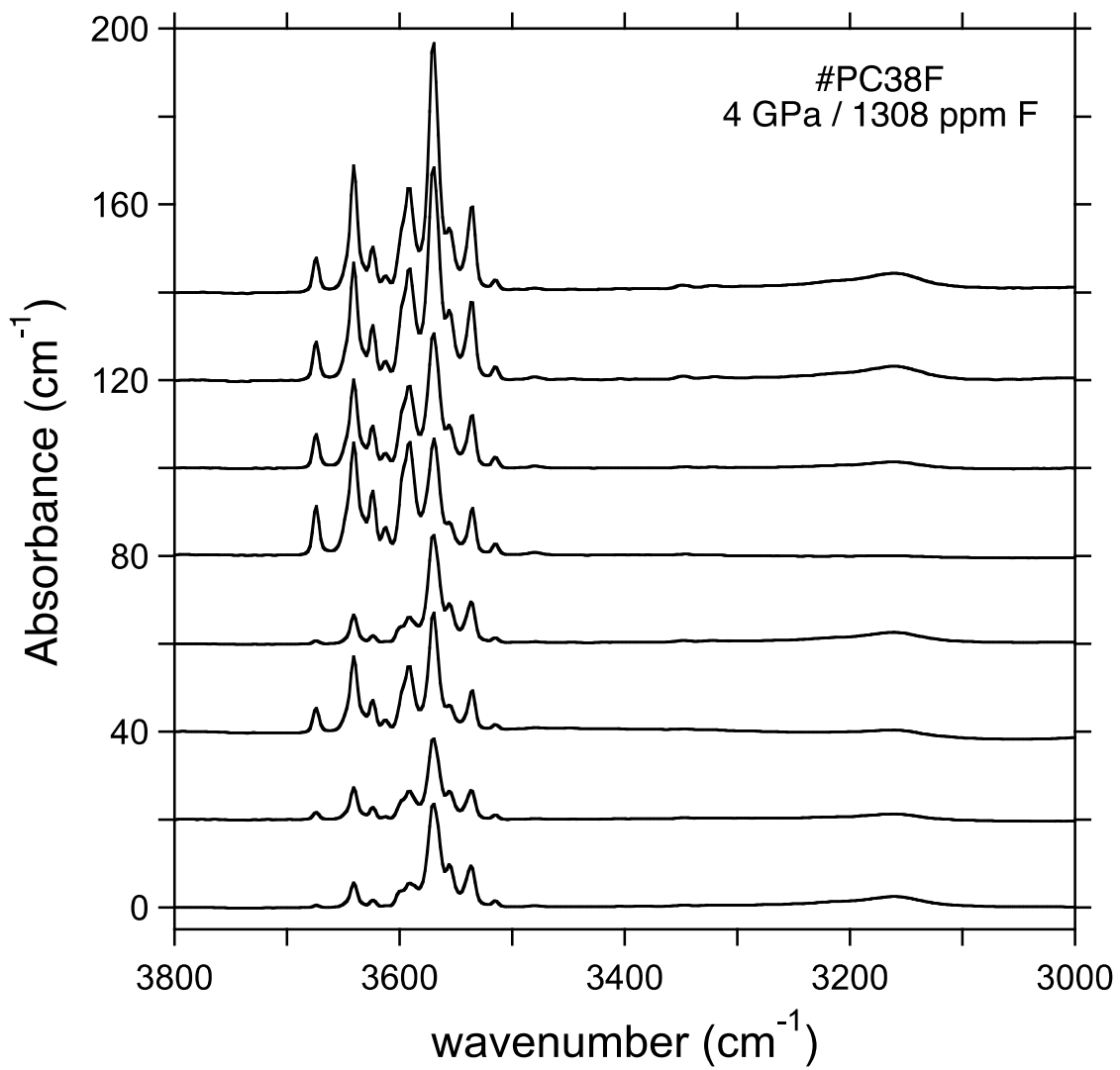


43
44 **Fig. 1.**
45



46 Fig. 2.

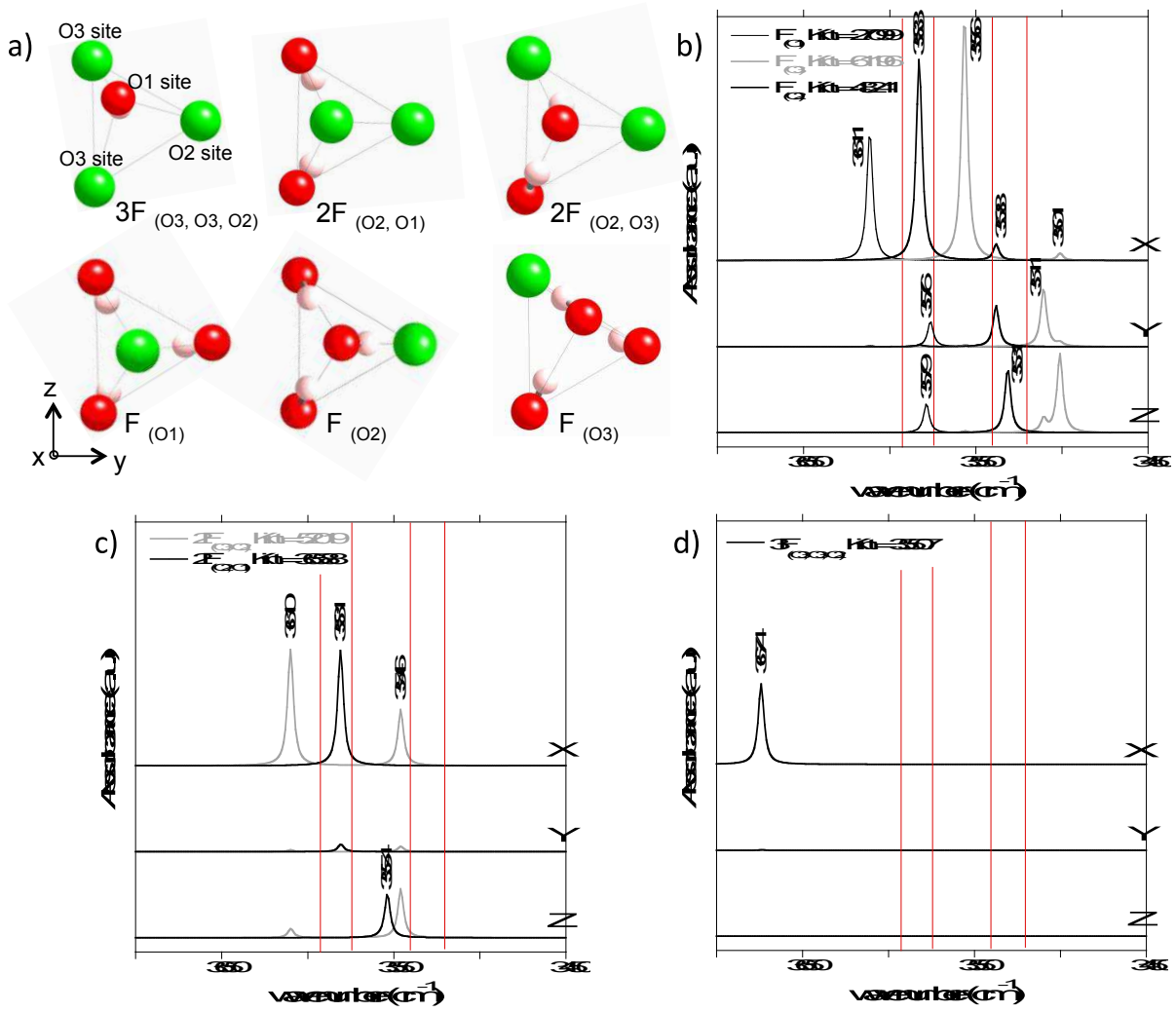
47



48

49 **Fig. 3.**

50



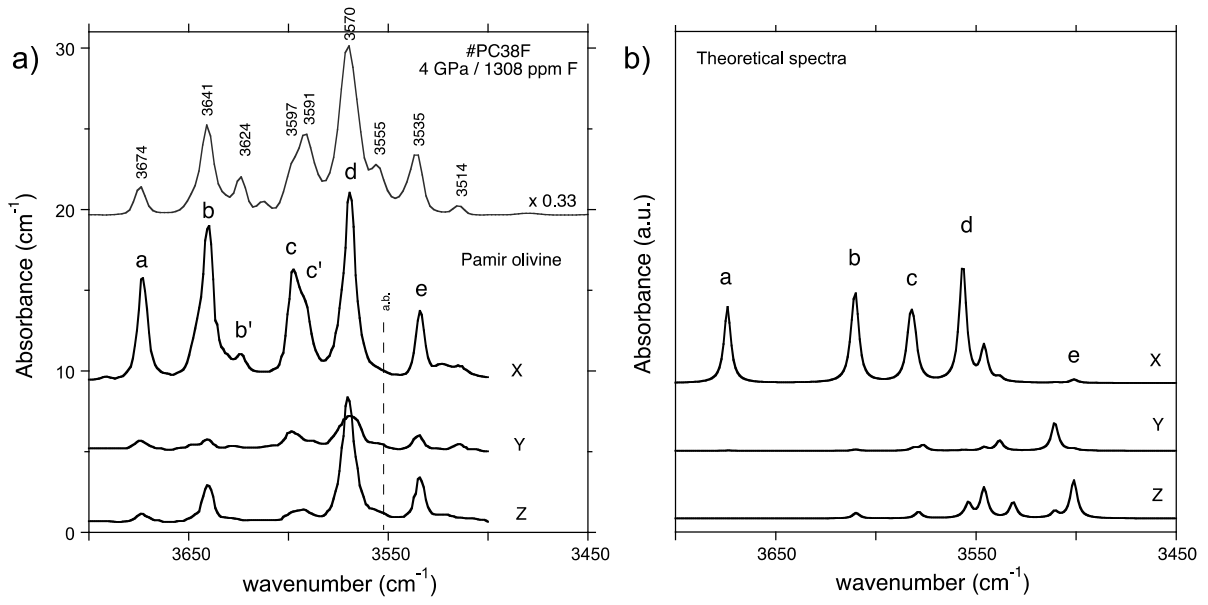
51

52 **Fig. 4.**

53

54

55

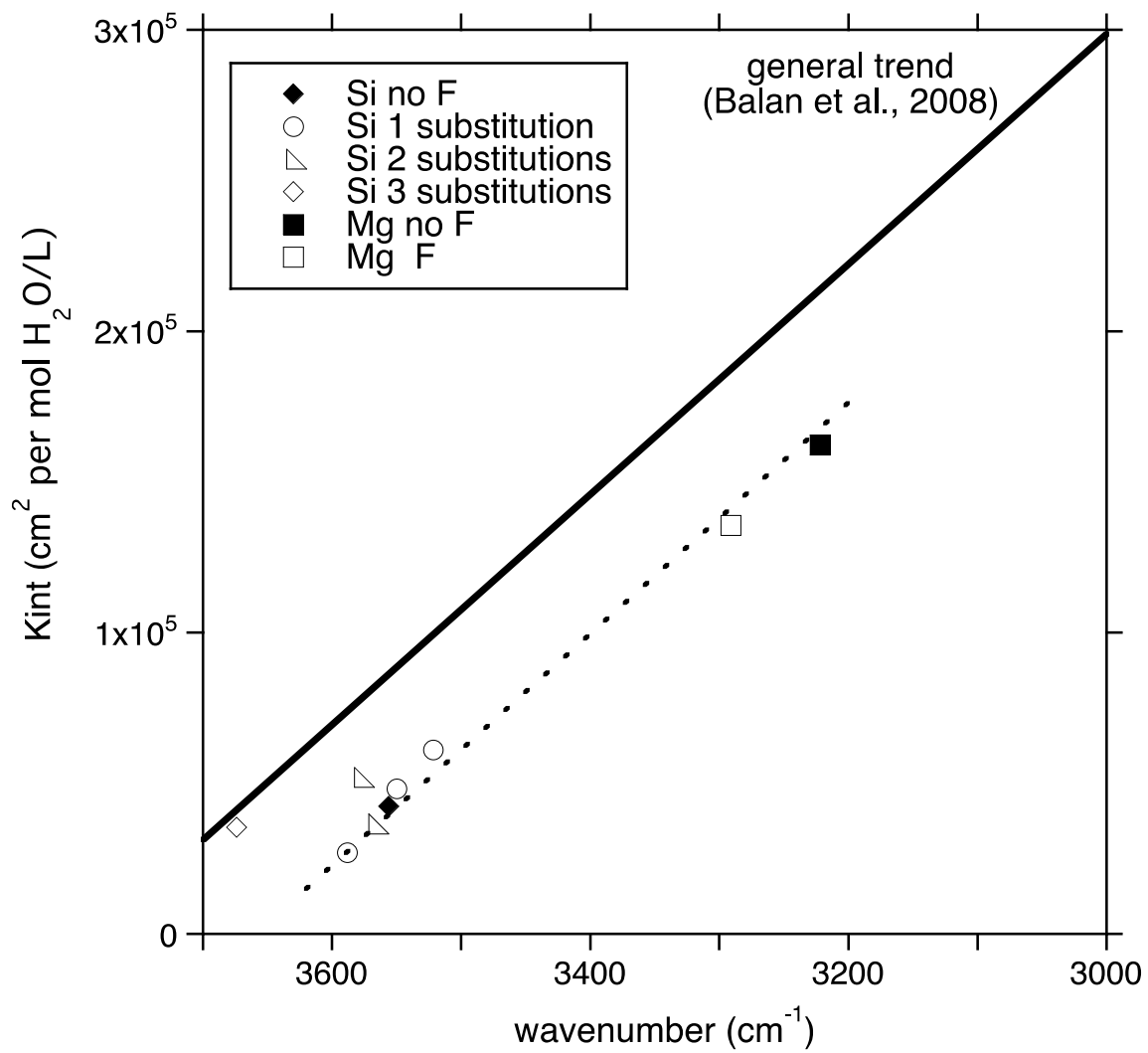


56
57 **Fig. 5.**

58

59

60



61

62 **Fig. 6.**

63